



香港城市大學
City University of Hong Kong

專業 創新 胸懷全球
Professional · Creative
For The World

CityU Scholars

Digital channel-enabled distributed force decoding via small datasets for hand-centric interactions

Tang, Yifeng; Li, Gen; Zhang, Tieshan; Ren, Hao; Yang, Xiong; Yang, Liu; Guo, Dong; Shen, Yajing

Published in:
Science Advances

Published: 24/01/2025

Document Version:
Final Published version, also known as Publisher's PDF, Publisher's Final version or Version of Record

License:
CC BY

Publication record in CityU Scholars:
[Go to record](#)

Published version (DOI):
[10.1126/sciadv.adt2641](https://doi.org/10.1126/sciadv.adt2641)

Publication details:
Tang, Y., Li, G., Zhang, T., Ren, H., Yang, X., Yang, L., Guo, D., & Shen, Y. (2025). Digital channel-enabled distributed force decoding via small datasets for hand-centric interactions. *Science Advances*, 11(4), Article eadt2641. <https://doi.org/10.1126/sciadv.adt2641>

Citing this paper

Please note that where the full-text provided on CityU Scholars is the Post-print version (also known as Accepted Author Manuscript, Peer-reviewed or Author Final version), it may differ from the Final Published version. When citing, ensure that you check and use the publisher's definitive version for pagination and other details.

General rights

Copyright for the publications made accessible via the CityU Scholars portal is retained by the author(s) and/or other copyright owners and it is a condition of accessing these publications that users recognise and abide by the legal requirements associated with these rights. Users may not further distribute the material or use it for any profit-making activity or commercial gain.

Publisher permission

Permission for previously published items are in accordance with publisher's copyright policies sourced from the SHERPA RoMEO database. Links to full text versions (either Published or Post-print) are only available if corresponding publishers allow open access.

Take down policy

Contact lbscholars@cityu.edu.hk if you believe that this document breaches copyright and provide us with details. We will remove access to the work immediately and investigate your claim.

ENGINEERING

Digital channel-enabled distributed force decoding via small datasets for hand-centric interactions

Yifeng Tang^{1,2}, Gen Li¹, Tieshan Zhang¹, Hao Ren¹, Xiong Yang², Liu Yang², Dong Guo¹, Yajing Shen^{2,3*}

Tactile interfaces are essential for enhancing human-machine interactions, yet achieving large-scale, precise distributed force sensing remains challenging due to signal coupling and inefficient data processing. Inspired by the spiral structure of *Aloe polyphylla* and the processing principles of neuronal systems, this study presents a digital channel-enabled distributed force decoding strategy, resulting in a phygital tactile sensing system named PhyTac. This innovative system effectively prevents marker overlap and accurately identifies multipoint stimuli up to 368 regions from coupled signals. By integrating physics into model training, we reduce the dataset size to just 45 kilobytes, surpassing conventional methods that typically exceed 1 gigabyte. Results demonstrate PhyTac's impressive fidelity of 97.7% across a sensing range of 0.5 to 25 newtons, enabling diverse applications in medical evaluation, sports training, virtual reality, and robotics. This research not only enhances our understanding of hand-centric actions but also highlights the convergence of physical and digital realms, paving the way for advancements in AI-based sensor technologies.

INTRODUCTION

The tactile interface is one of the most critical elements in intelligent human-machine interactions, allowing us to acquire large-scale tactile information from the surroundings and further give feedback to the machines (1–5). As one of the most direct physical extensions of our consciousness, our hands serve as the primary source of nuanced tactile sensations and function as intelligent tools for crafting and using objects in the physical realm (6). In addition, hand-centric interaction devices, such as joysticks, mice, keyboards, and touchpads, are also regarded as a major method to bridge the gap between human beings and the virtual world (7, 8). Regrettably, despite the critical role of the hand, decoding the strength and distribution of the forces generated by hands is still challenging, which has significantly impeded progress in various fields, such as precise medical treatment (9), efficient sports training (10), virtual reality (VR) manipulation (11, 12), robotics (13–15), and more.

For centuries, the hydraulic, pneumatic, and mechanical dynamometers (16) were the commonly used methods for assessing the force exerted by the human hand, but they can only provide information of maximum force, lacking spatial and temporal details (table S1). Recent advances in soft tactile skin provide opportunities for capturing force distribution, primarily through array-based [piezoresistive (17, 18), capacitive (2, 15, 19), piezoelectric (20), triboelectric (12, 21), magnetic (14), etc.] transductions and vision-based [Gelsight (22, 23), Tactip (24), TacLINK (25, 26), Insight (27), etc.] techniques. However, the electrical wire array-based method faces reliability issues due to material's sensitivity to environmental factors (temperature, humidity, electrical and magnetic fields) (14, 28, 29) and cross-talk problems (15, 21, 25), leading to reduced accuracy in large-scale contacts. While the optical-based method offers higher robustness by eliminating messy wires, they encounter accuracy issues in multiple large-areas

contacts (25, 27, 30) and have a limited sensing range, often hindered by easily occluded markers (22, 24–26, 31, 32) and/or usually requiring massive datasets (26, 27, 33). Moreover, the information obtained from almost all these soft tactile sensors is inherently the analog signals coupled from several unknown loading sources, making the force decoding very complicated, especially for forces applied from multiple points over a large area, just as hand grip force.

This study introduces a digital channel-enabled hand force sensing and processing strategy and then develops a phygital tactile sensing system (PhyTac) inspired by the decoding principles of touch neuronal systems (34, 35) and the spiral structure found in leaves of rosette plants (36–39) (*Aloe polyphylla*, *Aloe juvenna*, etc.) (Fig. 1). We achieve the highest marker density on record in parallel-type sensing surfaces and successfully decode the location of the loading [key nodes of interest (KOI)] from coupled mass signals, offering physically meaningful high-quality data. Our proposed physical model-enhanced neural network (FEM-NN) demonstrates the capability to reconstruct the distributed force map with high accuracy (0.11 N, 97.7% accuracy) within a large sensing range (0.5 to 25 N for a single point) using just a small dataset (45 KB). The capability of PhyTac in constructing the spatial-temporal hand force maps enables versatile applications, including finger and palm force evaluation, dynamic hand monitoring in tennis playing, VR manipulation, and human-robot interaction.

RESULTS

Bioinspired digital channel and spiral maker arrangement

The PhyTac (Fig. 1 and fig. S5) primarily comprises a bioinspired outer shell with receptor arrays, a polarizing linear light source positioned along the central axis, a top-mounted camera for motion capture, and connectors facilitating the integration of all components. The outer shell is cylindrically shaped to facilitate interaction, as the cylinder closely approximates the form of most handles in human life (40). To enhance reliability and robustness, we opt for optical signals as the sensory field to decode force-caused deformation, thereby eliminating the need for cumbersome wire arrays and

¹The Robot and Automation Center and the Department of Biomedical Engineering, City University of Hong Kong, Hong Kong, 999077, China. ²Department of Electronic and Computer Engineering, Hong Kong University of Science and Technology, Hong Kong, 999077, China. ³Center for Smart Manufacturing, Hong Kong University of Science and Technology, Hong Kong, 999077, China.

*Corresponding author. Email: eeyajing@ust.hk

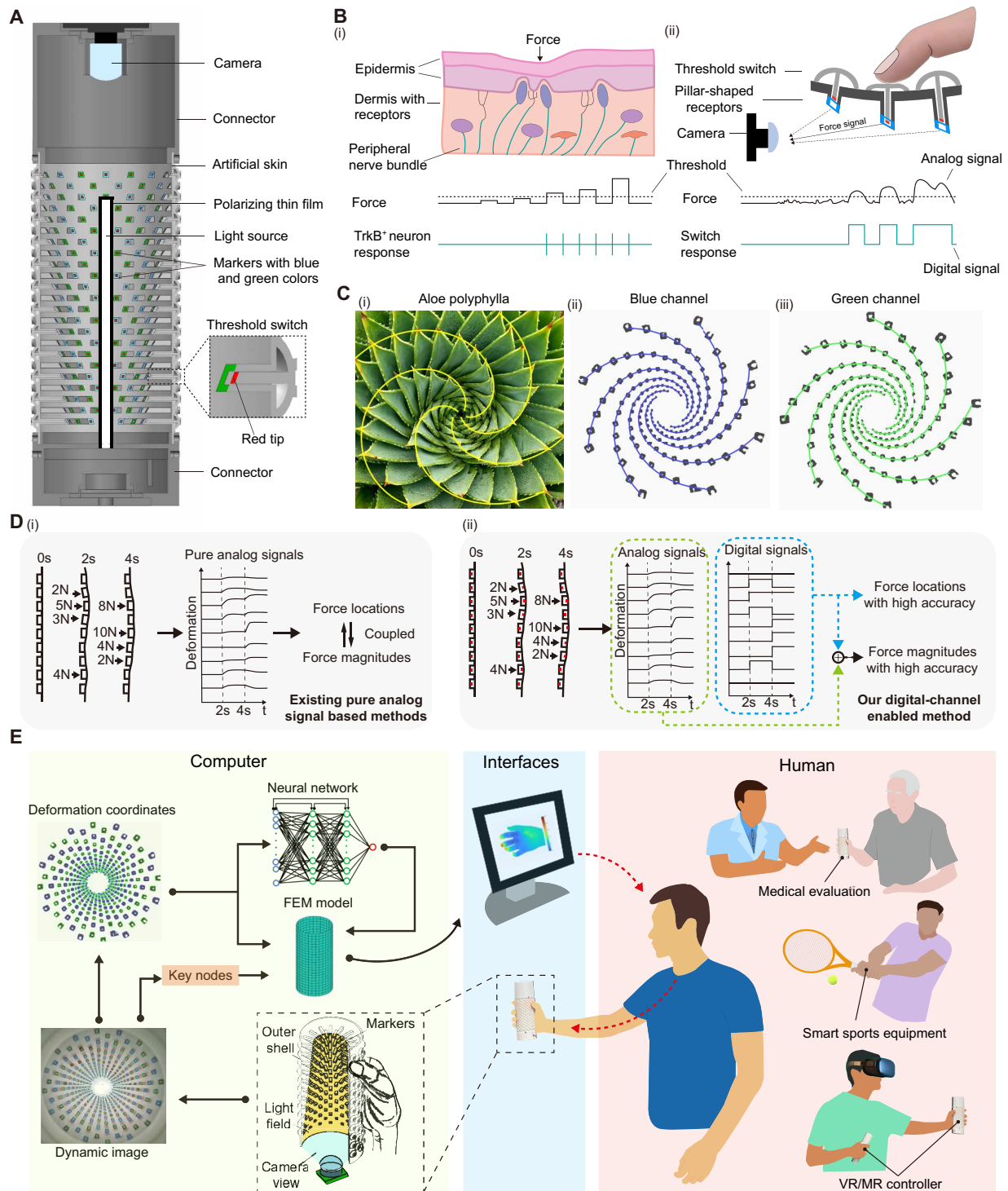


Fig. 1. Schematic illustration of the digital channel enabled phygital tactile system for large scale and precise distributed force sensing with ultrasmall datasets. (A) Cutaway view of the overall structures and components of the PhyTac. [(B), i] The structure of normal human skin and the deformation when force presses the skin (top). The illustration of TrkB⁺ neuron response when force is applied (bottom). [(B), ii] The detailed structure of the outer shell and the deformation when the finger presses the outer shell. Only the middle threshold switch is activated (top). The illustration of switch response and the generation of digital signals when force is applied (bottom). [(C), i] The spiral phyllotaxis of the *Aloe polyphylla*. Photo courtesy of C. Thorogood. [(C), ii] The biomimetic spiral arrangement of markers in the blue channel. [(C), iii] The biomimetic spiral arrangement of markers in the green channel. (D) Comparison of conventional pure analog signal methods and our digital channel enabled method. Force locations and force magnitudes are coupled with each other in pure analog signals [(D), i]. Force locations are decoded by digital signals with high accuracy and help reconstruct force magnitudes [(D), ii]. (E) PhyTac for human-machine interaction by measuring the hand force distribution, such as for medical evaluation, smart sports training, and VR.

rendering them minimally susceptible to environmental changes, such as temperature and humidity (41). The light source consists of a linear chip-on-board (COB) light strip with covered polarizing film, effectively eliminating unwanted refraction and uniformly projecting light onto all markers (fig. S6). Each receptor on the outer shell is designed as an independent unit, sensing the force applied in its vicinity. The extended height of each receptor gradually increases (ranging from 0.5 to 11.5 mm) away from the camera to prevent image blocking along the depth direction (Fig. 1A).

The state-of-the-art soft tactile sensors (12, 14, 18, 25, 27) face challenges in acquiring accurate force information when the load is applied on multiple points in a large area (Fig. 1Di), even massive datasets and complex algorithms are used. The reason is that the load-caused deformation in the surrounding area is quite complex, always resulting in coupled analog signal mixing by several unknown loading sources (locations, magnitudes, etc.), as illustrated in Fig. 1Di. The TrkB⁺ is a kind of sensory neuron in skin, producing spiking signal that exhibits on and off responses to tactile indentation (34, 35). This on-off digital property allows TrkB⁺ to lonely encode small threshold forces and help localize the stimulus. Inspired by the working principle of TrkB⁺ neurons, we deploy soft bowl-shaped threshold switches on the outer shell of PhyTac to output “on” and “off” digital signals (Fig. 1Bii), which can not only encode threshold forces but also help localize the loading points. When the multiple-point load is applied on the PhyTac, only the loading point will activate the switch to extend the red tip although numerous receptors are being deformed (Fig. 1B, i and ii). Then, the corresponding receptors to the activated switch will be counted as the KOI denoting the load location. Consequently, by taking the location of the applied force as preknowledge, the force magnitudes can be calculated more easily and accurately, as illustrated in Fig. 1Dii. The criterion of threshold is to filter out unwanted disturbances from surrounding stimuli. In this case, we set a force threshold of 0.5 N for the switch through mechanical design. Note that the threshold is adjustable for different applications.

Recognizing and tracking motion objects in three-dimensional (3D) space is another formidable challenge in image processing due to static and dynamic occlusions of light paths, as well as nonuniform light environments with highlights, shadows, etc. (42). For camera-based sensors, despite the perpendicular-type sensing surface (perpendicular to the optical axis of camera) can have a high marker density, the marker density of parallel-type sensing surfaces is still low due to easily occluded markers (fig. S7), resulting in small sensing range and limited resolution. For the measurement of the hand force, the sensing surface should be parallel to the optical axis, in which case it is very difficult to increase marker density. Phytologists disclosed that the spiral pattern of rosette plants, such as *Aloe polyphylla*, is selected by evolution to avoid light path occlusion and maximize sunlight capture benefits (36–39). This smart strategy can optimize the light path arrangement by avoiding leaf occlusion or self-shading, which is very instructive to the camera-based sensor design (fig. S8). To tackle the marker occlusion problem in 3D space, we lay out the receptors in a 3D spiral distribution, mimicking the leaf structure of *Aloe polyphylla* (Fig. 1C). In addition, by incorporating color distinction—using two spirals with blue and green colors, respectively—we achieve a remarkable marker density up to 1.63/cm², the highest record by far in vision-based sensors with parallel-type sensing surfaces (table S2). Furthermore, even with such a high density, we successfully avoid marker fusion at different

depths during motion, achieving high-accuracy tracking with a root mean square error (RMSE) of only 0.18 mm.

Figure 1E illustrates the comprehensive working process of PhyTac as the interactive interface, encompassing the reception of the hand force signal to the output signal, bridging the real and virtual world. Briefly, when the PhyTac receives the force from the hand, its outer shell undergoes deformation, and the motion of each receptor is captured by the camera. Subsequently, leveraging the identified key nodes and the displacements of all markers as input, the FEM-NN accurately establishes the mapping relationship between marker displacements and force distribution. This process allows the system to obtain the reconstructed tactile force information from the hand, ultimately facilitating advanced human-machine interaction across a broad spectrum of applications, such as evaluating the functionalities of muscles/nerves/bones of hands in clinical medicine, testing distributed force loading in sports, and manipulating objects precisely in the virtual world among other possibilities.

Distributed force decoding principle and process

Figure 2A presents the schematic of the two-column spirally arranged markers (spiral angle α : 50.5°, radius R : 30 mm) colored blue and green. When the hand grasps the PhyTac (Fig. 2B), the outer shell's surface deforms, and the surrounding receptors generate displacement accordingly. To represent the marker's motion, we establish a 2D coordinate system at point O , with i as the axial direction and j as the circumferential direction (Fig. 2Bi). The markers' displacements in the image plane presented, denoted as d_{ij} (Fig. 2Bii), can be measured through image processing and then translated into real displacement D_{ij} (Fig. 2Biii) in the world coordinate system XYZ (Fig. 2A). Consequently, the complete displacement matrix D can be obtained as illustrated in Fig. 2Biv. The chromaticity diagram (CIE 1976) and point cloud in the YCbCr color space demonstrate that the selected three distinctly different colors (blue, green, and red) are well-separated in the digital color space, facilitating easy segmentation in image processing (Fig. 2, C and D).

When the local force surpasses the threshold, the red tips of the threshold switch extend outward and are identified through the red channel (Fig. 2F and movie S1). The markers, whose threshold switches are activated in the red channel, are signified as logic “1,” and the other markers are signified as logic “0,” forming a digital channel that represents the spatial distribution of critical force. This digital channel has a binary form: $b_1 b_2 \dots b_n$, where b is a binary number 0 or 1, and n represents the total number of nodes. Then, all logic “1” nodes are defined as KOI: = $\{r_i | i = 1, \dots, m\}$, where r_i is the index of key node and m is the number of key nodes. During the deformation process, although spatial distribution of force changes every frame, the digital channel can obtain the spatial distribution from coupled analog signals efficiently, assuring the accuracy of force estimation and reducing computational resources when there is no logic “1” detected. By contrast, the pure analog signal-based methods need complex algorithms and massive datasets to decode force locations, not only facing challenges in large-scale contacts but also consuming more computational resources.

Simultaneously, the positions of all markers in the image coordinate are recognized through the green and blue channels (Fig. 2Fiii) and are dynamically tracked by using a k-medoids-based coordinate matching method (fig. S9). Subsequently, the marker coordinates on the 3D outer shell are constructed using a coordinate geometrical mapping function (fig. S10 and note S1). Consequently,

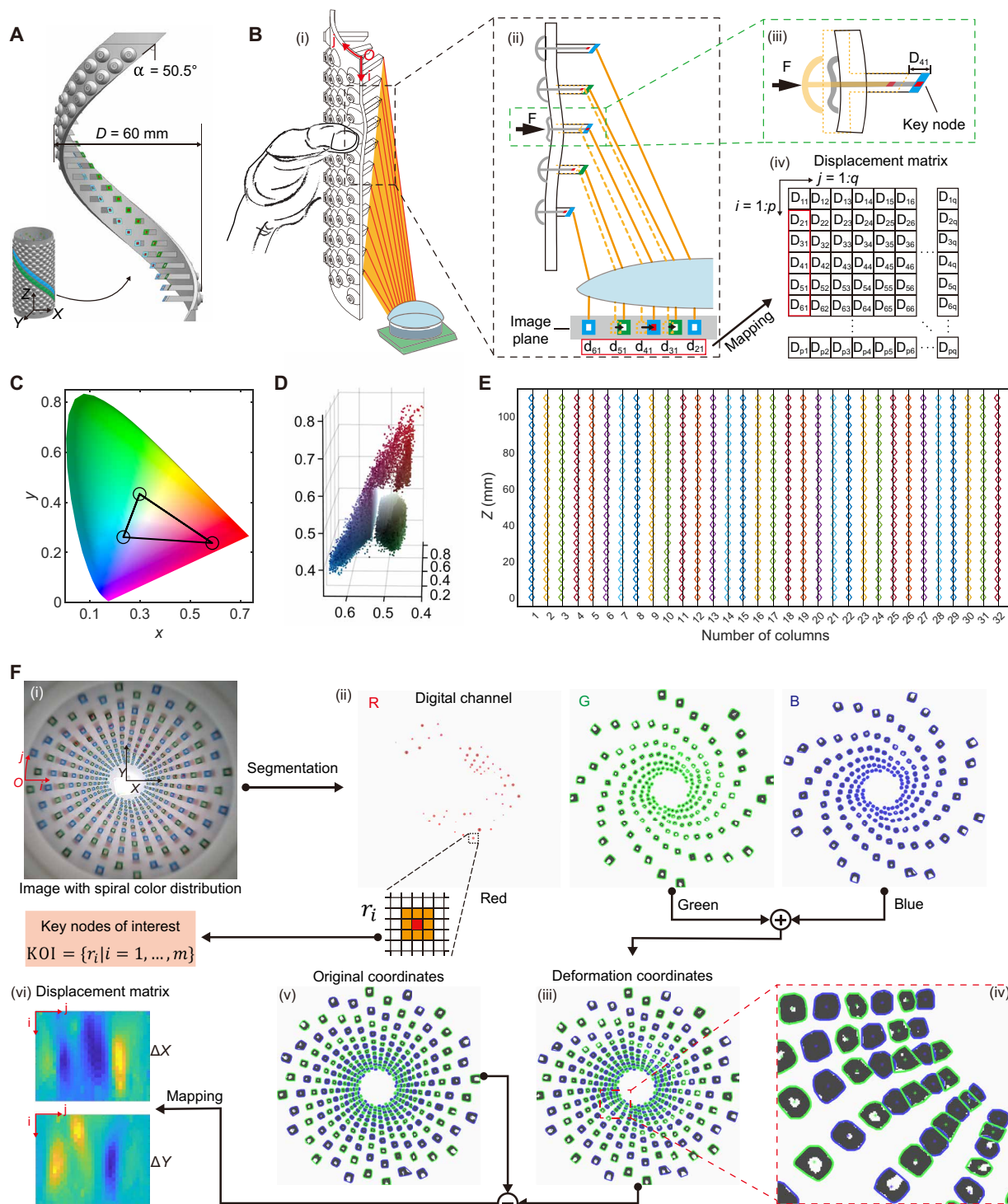


Fig. 2. Design and working principle of the PhyTac with spirally arranged receptors and digital channels. (A) The minimum spiral element of the PhyTac. (B) Schematic illustration showing the relationship between applied force and displacement matrix of markers. [(B), i] Cutaway view of the PhyTac measuring the hand grip force. [(B), ii] Only the receptors at the loading point will be activated though several receptors are deformed. [(B), iii] Enlarged image of the activated receptors, named KOI. [(B), iv] Mapping of displacement matrix. (C) The selected colors in chromaticity diagram. (D) Point cloud in YCbCr color space. (E) Original coordinates unwrapped in the circumferential direction. (F) The procedures of data processing. [(F), i] The image with spiral color distribution. [(F), ii] Segmented red channel containing the digital information of the force location (KOI), and the blue and green channels containing the information of marker displacement. [(F), iii] Deformation coordinates of all markers. [(F), iv] Enlarged image shows the spiral arrangement can address marker fusion problem and segment overlapped markers effectively. [(F), v] Original coordinates of all markers. [(F), vi] The displacement matrix in X and Y directions.

the displacement matrix D is obtained by accounting for the difference between initial coordinates and deformed coordinates (Fig. 2Fvi), providing the magnitude distribution of all forces.

It is also noteworthy that the bioinspired spiral structure allows the camera to capture to the maximum extent by preventing marker fusion. This feature is beneficial as it ensures clear segmentation of markers and accurate recognition of corresponding coordinates. As illustrated in Fig. 2Fiv, even when marker overlap occurs due to high marker density and large deformation, the bioinspired spiral structure enables clear segmentation of marker contours. For comparison, markers fuse together when using a traditional structure (fig. S11), leading to coordinate errors and force inaccuracies. Experimental results demonstrate that the precision of reconstructing original coordinates in the initial image is up to 0.18 mm (RMSE), as shown in Fig. 2E. This indicates that the reconstructed coordinates (diamond marks) almost coincide with the reference coordinates (black line).

Physical model-enhanced neural network

Machine learning has proven to be a powerful method for image-based force construction (22, 27, 33), leveraging its strength in non-linear fitting, end-to-end mapping procedures, etc. However, in addition to big data processing caused inefficiency, another significant drawback of this type of data-driven approach is the absence of underlying physics. Even with extensive data, it may yield arbitrary extrapolating when faced with situations beyond the scope of the training data, because, in real practice, it is difficult to collect comprehensive training data for complex contacts involving different contact locations and magnitudes. Therefore, we propose an approach integrating the mechanical model of the outer shell into neural network training, named FEM-NN, aiming to circumvent the need for massive datasets and mitigate inaccuracies arising from arbitrary extrapolation.

We establish the physical model of the outer shell using finite element theory (43) taking into account its thin thickness (0.8 mm). As illustrated in Fig. 3Bi and fig. S12, the outer shell is uniformly discretized into a mesh with N_e elements and N_n nodes, where the mesh size is determined on the marker density to align dimensions. The basic shell element is considered a small rectangular domain, and its length and width are computed on the basis of the geometrical parameters of the outer shell. According to the physical constraints of PhyTac, the nodes in the top layer and the bottom layer are treated as fixed nodes, while the remaining nodes are considered as free nodes with five degrees of freedom (5-DOF), including three displacements and two rotations about the Z axis. Applying the principle of virtual work, the state equation of the element in static equilibrium (43) can be presented as follows

$$\iint_A \delta \hat{\mathbf{e}}^T \hat{\boldsymbol{\sigma}}^T dA = \iint_A \delta \mathbf{u}^T \mathbf{t} dA + \delta \mathbf{u}^T \mathbf{f} \quad (1)$$

where the left side represents the internal virtual strain energy, and the right side represents the external virtual work. Here, \mathbf{u} is the virtual displacement vector, $\hat{\mathbf{e}}$ is the strain vector, $\hat{\boldsymbol{\sigma}}$ is the stress vector, \mathbf{t} is the surface load, and \mathbf{f} is the force vector.

By substituting the relevant variables to Eq. 1, the state equation can be simplified to $k_e \cdot \mathbf{u}_e = \mathbf{f}_e$, where k_e , \mathbf{u}_e , and \mathbf{f}_e are the element stiffness matrix, element displacement vector, and element force vector (note S2). Then, the relationship between displacements and external force can be obtained as $K \cdot \mathbf{U} = \mathbf{F}_p$ by assembling all

elements into the global system, where K , \mathbf{U} , and \mathbf{F}_p are the global stiffness matrix, global displacement vector, and global force vector. K is known from the finite element model (FEM), and \mathbf{U} can be derived from the displacement matrix mentioned earlier, allowing for the computation of external forces \mathbf{F}_p .

Figure 3 illustrates the working mechanism of the FEM-NN. Following the principle of the four-node rectangular element of finite element theory (43), the displacement/force of a given node i is influenced by the surrounding eight nodes. To compensate for the missing physics (44, 45) of FEM (nonlinear effects, mesh density/quality, order errors, and material errors), we select $nn_i = [\mathbf{u}_i z_i]^T$ as the training input and k_i as the training output for a cascade neural network (Fig. 3A), where the displacement vector $\mathbf{u}_i \in \mathbb{R}^9$ represents the displacements of node i and its eight surrounding nodes, the scalar z_i represents the height of the node i in the global coordinate system, and the scalar k_i is the augmented local stiffness. Then, the training data were collected experimentally using a 3-DOF automatic test platform comprising three types of grippers, which can make different contact distributions (Materials and Methods and figs. S13 and S14). Because input and output selections of neural network are also based on the principle of FEM, the overall training data are physically meaningful high-quality data. Once the network is trained, consequently, k_i ($i = 1, \dots, m$) can be calculated through the corresponding input $[\mathbf{u}_i z_i]^T$ by scanning the KOI in the displacement matrix D , and the augmented stiffness matrix $\delta K(\mathbf{U})$ can be obtained as

$$\delta K(\mathbf{U}) = \begin{bmatrix} k_1 & \cdots & 0 \\ \vdots & \ddots & \vdots \\ 0 & \cdots & k_m \end{bmatrix} = \begin{bmatrix} g(nn_1) & \cdots & 0 \\ \vdots & \ddots & \vdots \\ 0 & \cdots & g(nn_m) \end{bmatrix} \quad (2)$$

where the $g()$ represents the trained cascade neural network, $\delta K()$ represents the procedures of circularly scanning the KOI of the displacement matrix and extracting the corresponding input nn_i from the displacement matrix, and m is the number of KOI. Last, the external forces \mathbf{F} can be reconstructed by adding the FEM part and the augmented part (neural network) (Fig. 3B and note S3)

$$\mathbf{F} = [(K + \delta K(\mathbf{U})) \cdot \mathbf{U}] \quad (3)$$

Benefiting from the C^0 continuity of shell element in the finite element model, the applied force at any arbitrary position on the outer shell can be theoretically calculated by interpolation.

Distributed force measurement based on small datasets

We calibrate the FEM-NN model and compare the force reconstruction accuracy of FEM-NN (Fig. 3, C and D) with the physical model-based method (FEM) and convolutional neural network-based method (CNN) using single-point contacts and multiple-point contacts (Materials and Methods and note S5). It indicates that the accuracy of FEM-NN remains remarkably high across the entire force range (0.5 to 25 N) with an average force magnitude error of ~ 0.11 N and an average relative error of only 2.3%. In comparison, the average relative error by FEM is around 18%, particularly high (49.0%) when the applied force is small (< 5 N). The overall accuracy of CNN is approximately 93.0%, which approaches the accuracy of FEM-NN. But note that the dataset of CNN includes 3909 samples (> 1 GB), over six times larger than the needed dataset of our FEM-NN (598 samples, 45 KB), and the accuracy of CNN would reduce largely to 48% if using the same small imagesets (fig. S15).

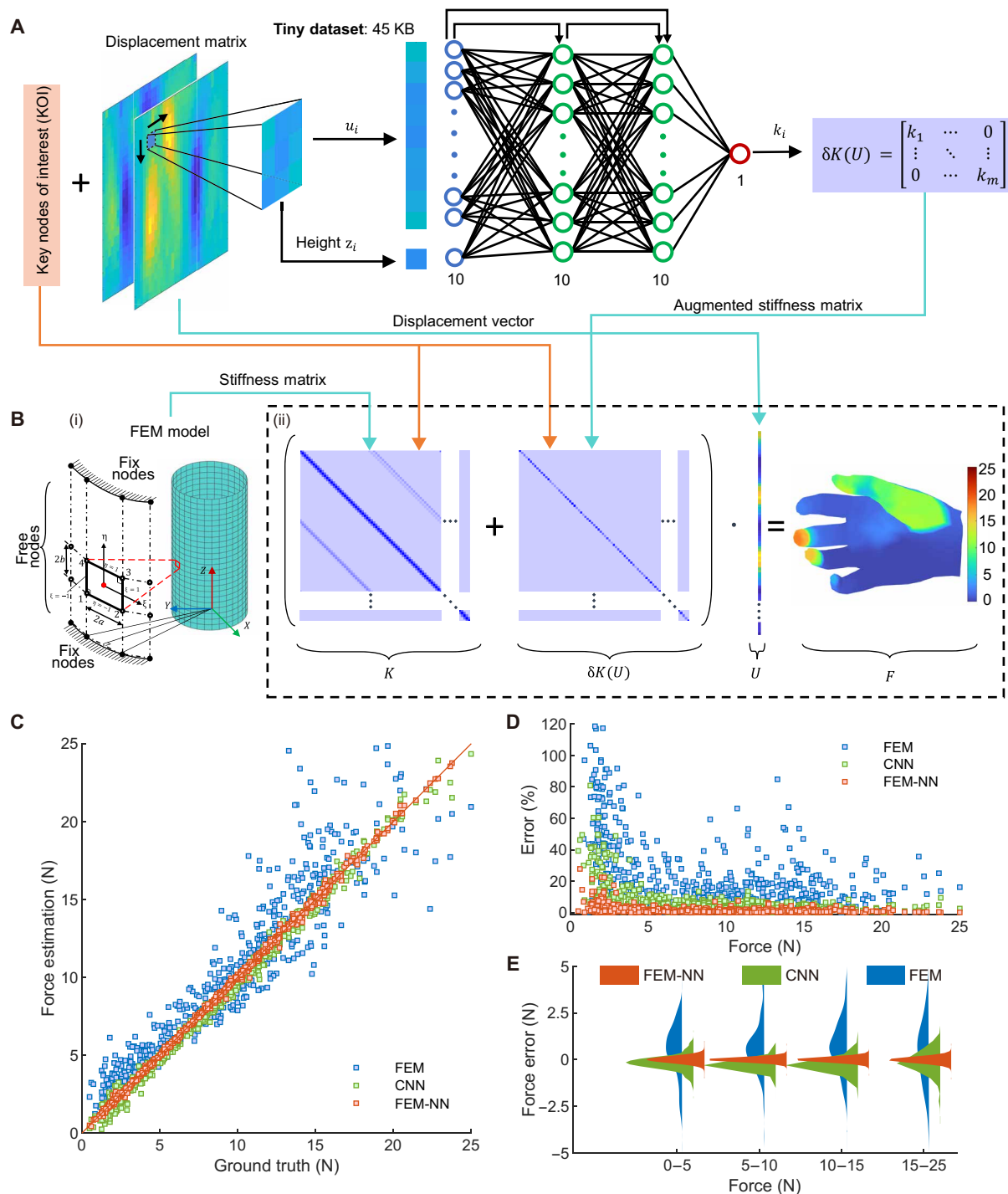


Fig. 3. Principle of FEM-NN and its superiorities in small dataset and high accuracy. (A) The architecture of FEM-NN with tiny dataset (45 KB). The inputs are KOI and displacement matrix, and the output is augmented stiffness matrix. (B) FEM-NN based force reconstruction algorithm. [(B), i] The finite element model of the PhyTac, including the geometry of four-node rectangular element (left) and the mesh topology (right). [(B), ii] The force reconstruction algorithm, including the stiffness matrix, augmented stiffness matrix, displacement vector, and reconstructed force distribution on hand. (C) The statistical summary of the force estimation accuracy of three different methods (FEM, CNN, and FEM-NN). (D) The relative force error distribution of FEM, CNN, and FEM-NN along force magnitude. (E) The quantitative evaluation of the absolute force error distribution of FEM, CNN, and FEM-NN in different force ranges.

Figure 3E further demonstrates that the quantitative distribution of absolute force errors by FEM-NN is concentrated around 0 N with a small SD (<0.16 N) over the entire force range. This performance is superior to the other two conventional methods, which exhibit large means (>0.35 N) and large SD (>0.28 N).

To better evaluate the performance of our method in real scenarios, we also conduct real hand grip experiments in different grip orientations, positions, or directions, applying forces in a large range from 0.5 to 25 N (fig. S16). The overall accuracy of real hand grip is at the same level as the data from the automated platform (fig. S17), which can validate the generalizability of our FEM-NN model. Furthermore, our device remains robust across different grip orientations and directions, as shown in figs. S18 to S20, due to the working mechanism not being affected by gravity. Then, the accuracy remains stable among different heights of 5 to 110 mm, with only a slight reduction of approximately $\sim 4\%$ at the narrow region near the bottom (105 to 110 mm) (fig. S18). Considering that the middle area (heights of 15 to 95 mm) is the most frequent contact area, the overall error is still within an acceptable error range. The results also clearly reveal that the majority of forces are distributed on fingertips and *musculus flexor pollicis brevis*, aligning with our intuitive experience in daily life (Fig. 3B, fig. S21, and note S4). Note that the sensing range from 0.5 to 25 N is only for one single point, so if applying force on multiple points, the maximum total force can be up to more than 200 N, and this large range will help our PhyTac applied on many applications, such as sports and VR. Repeated stability test over 1000 cycles was performed, and the PhyTac exhibits no signal drift or fluctuation during the cyclic tests (fig. S22).

It is worth noting that our FEM-NN model requires only a small dataset (just 45 KB) for training. The digital channel allows us to directly extract the location information of the load. Benefited from such high-quality data without interference, the searching space in FEM-NN can be finely constrained within the KOI and its surrounding eight markers' displacements, as shown in Fig. 3A. In contrast, the searching space of CNN is unconstrained and stochastic over the input images (original images or the entire displacement matrix) with thousands of dimensions. Compared with the conventional method, our approach reduces the number of training parameters by more than 2000 times, from 758.4K (CNN) to 351 (FEM-NN). Consequently, our method requires only minimal computing resources, and the training process can be completed within 1 min (fig. S23), a notable improvement compared to the several hours needed for other image-based deep neural networks.

The introduced physical model establishes a theoretical mechanical framework to connect the marker displacement and force magnitude and provides valuable prior knowledge that incorporates material, geometric, and mechanical properties of PhyTac. In real practice, because of the limitations of mesh density/quality, order errors, material errors, etc., the FEM model is usually with partially missing physics (44, 45), resulting in low accuracy. For this weakness, the FEM-NN model endorses the neural network with the powerful fitting ability, effectively compensating for the missing physics between the finite element model and the real-world model. The results verify that FEM-NN can better model the overall physics and guarantee the reasonability and reliability in force reconstruction. Note that the physical model is a little bit similar but not equal to the pretrain model, due to the stiffness matrix is derived from the mechanical model and does not need a training process.

Demonstrations for hand force estimation, the virtual world, and robot connection

The PhyTac provides a straightforward solution for estimating the strength and distribution of forces generated by hands (16), directly benefiting evaluation and treatment of various diseases (stroke, rheumatoid arthritis, etc.). In comparison to other potential solutions like gloves (17), our approach stands out for its robustness, ease of use, and unobtrusiveness. As depicted in Fig. 4A and movie S2, it adeptly recognizes dynamic changes in force distribution from all fingers and hands across different gripping postures and strengths. Intuitively, we observe that the largest force concentrates on the fingertips of the thumb when using the thumb and forefinger for grasping (Fig. 4Ai), shifts to the *musculus flexor pollicis brevis* when using three fingers (Fig. 4Aii), and appears in the middle finger and ring finger when using four fingers (Fig. 4Aiii). In addition, we note that the force distribution from our hand varies with different applied strengths to grasp the object. For instance, the largest force is primarily applied by the *musculus flexor pollicis brevis* in the case of high strength (Fig. 4Aiv), while the force is mainly contributed by the thumb and fingertips of the other fingers in the case of low strength (Fig. 4Av). These quantitative insights enhance our understanding of hand actions at a high-precision level. Furthermore, the precise grip force distribution contains many rarely decoded information, which suggests the conditions of hand joints and muscles, making it potentially applicable in the evaluation and treatment of various diseases, such as stroke (16), and rheumatoid arthritis (46).

The precise force production from different regions of the hands forms the foundation for most sports competitions. The advancements of PhyTac in distributed sensing ability and large sensing range position it as a smart sports instrument for quantitatively evaluating such actions. As depicted in Fig. 4 (B and C) and movie S3, the PhyTac, when installed on the tennis racket (fig. S24), can provide real-time dynamic force strength distribution from hands during tennis playing. Figure 4B illustrates that during forehand hitting, the applied force is primarily distributed in the forefinger, middle finger, and ring finger, along with their surrounding parts of the palm. The results in Fig. 4B (ii to iv) show that the largest force (23.9 N) occurs at +30 ms in the region of the forefinger, with the thumb and little finger contributing smaller forces (<10 N) in this process. In contrast, the backhand hitting (Fig. 4C) involves a different force distribution, with the thumb, ring finger, and little finger contributing more force. Specifically, the thumb produces the largest force (23.6 N) to hit the ball, while the ring finger and little finger appear to act as a fulcrum point in rotating the racket (Fig. 4C, ii to iv). Outputting at least two orders of magnitude larger parameters than traditional devices (47), our distributed force decoding device offers a scientific tool for deeper understanding of the interaction between plays and rackets, finally improving players' performance and preventing injuries (48).

We also demonstrate that PhyTac can enable precise VR manipulation by projecting force distribution from the real world to the virtual world. While in the real world, we can use different forces to grasp, hold, and crush objects like eggs, replicating these actions in the virtual world has been challenging due to the lack of a distributed force-based interaction interface. PhyTac can accurately transfer the produced force from different fingers to the virtual world, enabling force-induced manipulation, as shown in Fig. 4D and movie S4. The demonstrations illustrate that we can delicately hold

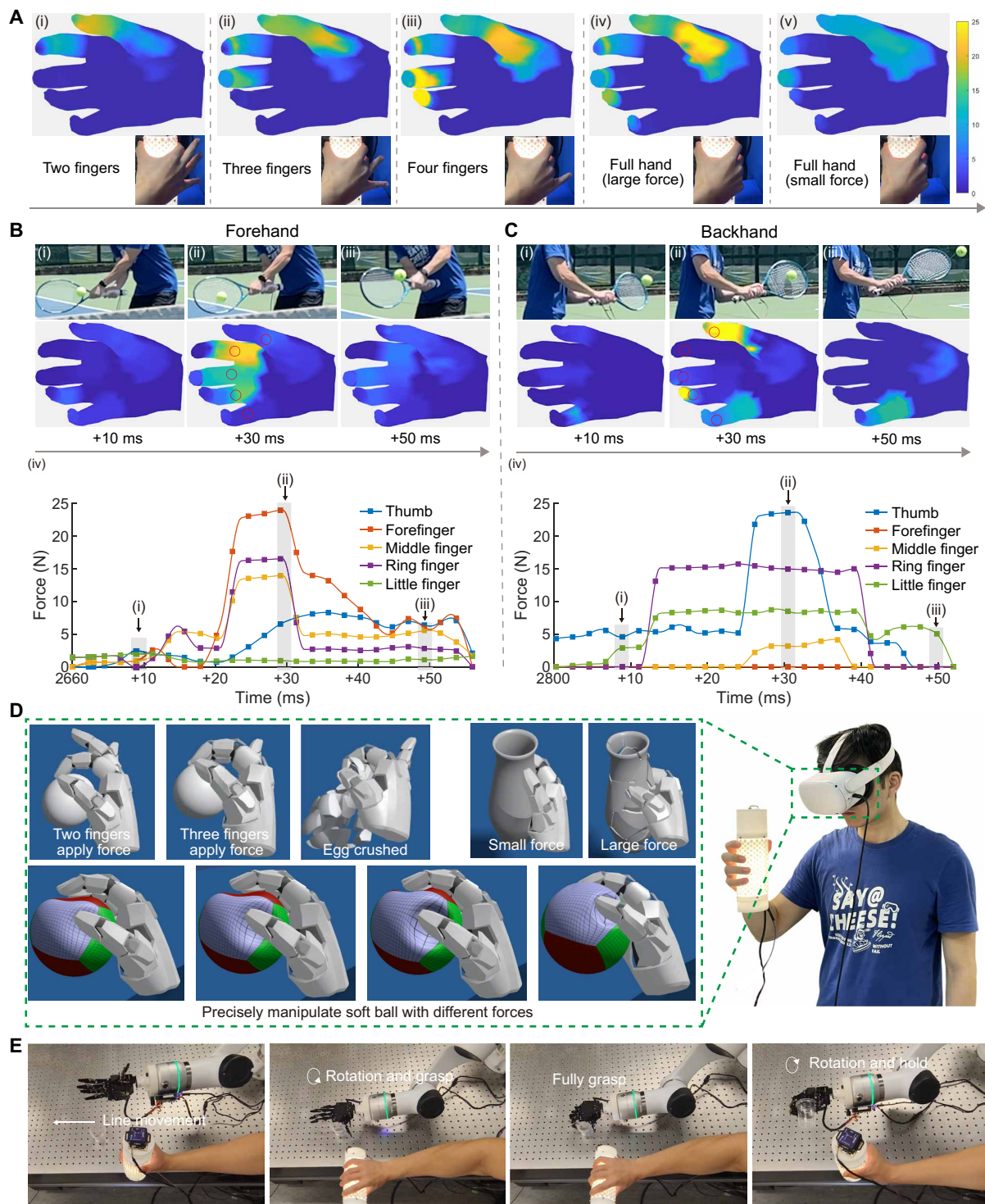


Fig. 4. Application demonstrations of PhyTac in multiple finger grasping, dynamic hand grip force measuring in tennis playing, VR interactions, and robot tele-operation. (A) Grasping the PhyTac using different numbers of fingers validates the capabilities of PhyTac for hand grip force measurement. (B) Force distributions in forehand tennis playing at prestroking [(B), i], stroking [(B), ii], and poststroking [(B), iii]. [(B), iv] Force changes of five points of fingers with time. (C) Force distributions in backhand tennis playing at prestroking [(C), i], stroking [(C), ii], and poststroking [(C), iii]. [(C), iv] Force changes of five points of fingers with time. (D) Precisely grasp, hold, crush, and deform objects in the virtual world by projecting the force from hand in the real world. (E) Using PhyTac to control the robot hand to grasp and move a thin plastic cup without collapsing.

an egg using a thumb and forefinger without crushing it or scratch it using three fingers when the total force exceeds the threshold (50 N). Similarly, we demonstrate the scratching of a vase (total force >80 N) and the manipulation of a softball (ranging from 5 to 20 N). Furthermore, leveraging PhyTac's excellent dexterity in 3D space, it can serve as a teleoperation interface by integrating the inertial measurement unit (IMU) to control the motion of a robotic finger for manipulation that is sensitive to gripping force. As demonstrated in Fig. 4E, we are able to control the robot finger to pick up, hold, and transfer a thin plastic cup without crushing (movie S5). Note that, different from existing methods (table S3), our device can directly control the force to avoid damaging objects, in addition to its lightweight and low cost. These features position PhyTac as a promising device to bridge the gap between the physical world, virtual world, and robots, with potential long-term impact in various fields, including prosthetic robot sensing, safety control, precise remote control of surgical robots, and human-robot interaction.

DISCUSSION

This research yields a digital channel-enabled distributed force decoding strategy and a robust tactile interactive system capable of reconstructing dynamic spatial-temporal hand force. In particular, the introduction of a digital channel to force decoding can extract the location of force from the coupled analogy signal, offering physically meaningful high quality training data and easing force reconstruction processing. The bioinspired spiral arrangement obtains the largest marker density on record in parallel-type sensing surfaces and overcomes the marker overlap issues in existing marker-based devices. Furthermore, the FEM-NN architecture can reconstruct the force with an ultrasmall dataset, not only addressing the arbitrary extrapolation and massive dataset challenges in force mapping but also paving notable concepts for the development of soft tactile sensors and AI algorithms. Two prototypes with different sizes validate not only the effectiveness of our strategies but also the excellent robustness and high accuracy. It is worth noting that, while the diameters of our prototypes are 40 and 60 mm, the design is easily adjustable to fit hands of various sizes. In addition to the cylinder geometry, our design framework is also compatible with other shapes, including planes, cones, cuboids, hemispheres, and curved surfaces (fig. S25). In addition to the camera-based tactile sensors, the concept of digital channel could also be applied to other types of distributed soft tactile sensors to overcome interference problems and accurately locate complex stimuli, especially in high-density arrays. While adding a layer of digital channel may complicate the fabrication process, it is also a viable option for researchers to improve distributed force accuracy. This work stands out from previous approaches (table S2) in terms of small datasets, large sensing range, large sensing area, and high accuracy, laying the groundwork for broader applications in VR, augmented reality, mixed reality, health care, sports, and robotics.

MATERIALS AND METHODS

Materials and fabrication of the PhyTac

A schematic illustration of the common fabrication process is depicted in fig. S26. The outer shell of PhyTac was fabricated by 3D printing, using a photosensitive resin material with excellent toughness (3D printer, lite600hd, Ningbo Zhechuang Technologies Co.

Ltd., China; material, C-UV 9400E, Wenext Technology Co. Ltd., China). The markers of the outer shell were manually colored using blue and green mark pen (bluemark pen: grasp 64; green mark pen: grasp 46, Wenzhou Jinma Stationery Manufacturing Co. Ltd., China). We selected thermoplastic polyurethane (TPU) elastomer (Hei-Cast 8400N, H&K Ltd., Japan) as the mouldable material for the soft threshold switch. Parts A and C of the TPU were combined in a weight ratio of 1:5, followed by stirring the mixture for 2 min. A vacuum pump was used to remove bubbles from the mixture for 5 min. Subsequently, the mixture of parts A and C was added into part B in a weight ratio of 6:1, and then the mixture was stirred for 30 s and bubbles were removed for an additional minute. All these processes were conducted at 25° to 35°C. The mixture was then injected into a prepared silicon mould and cured at 65°C for 1 hour. After demoulding, the tips of threshold switches were colored with a red mark pen (grasp 15). Threshold switches were then integrated into the outer shell using an adhesive (Loctite 406, Henkel AG & Co. KGaA, Germany). The COB light strip (Shenzhen Greethink Electronic Co. Ltd., China), polarizing films (Shenzhen Yijia Photo Products Co. Ltd., China), and 3D-printed light source skeleton were integrated using double faced adhesive tape. The connectors were fabricated using 3D printing from lite600hd. The camera used in tennis playing (KS1.3A142-GS, Shenzhen Jingcent Photo Products Co. Ltd., China) has a resolution of 640 × 480 and a frame rate of 480 fps, and the camera used for other cases (HF500, Shenzhen JRWT Electronic Co. Ltd., China) has a resolution of 2592 × 1944 and a frame rate of 30 fps. The connectors, camera, outer shell, and light source were assembled by screws.

Test platform for PhyTac calibration and data collection

Two test platforms are established to collect training data and validation data. The 3-DOF automatic test platform, used for PhyTac calibration and training data collection, is depicted in figs. S13 and S14. One DOF controls the Cartesian movement of the PhyTac along the Z axis using a linear screw actuator with a precision of 0.03 mm (Sheng Starr Transmission Technology Co. Ltd., China), and one DOF controls the rotation angle of PhyTac around Z axis using a closed-loop stepper motor (Dekesi Motor) with a precision of 0.0036°, and the final DOF controls the grasping depth of graspers using a bidirectional linear screw actuator with a precision of 0.06 mm. The graspers, indenters, and connectors were fabricated using 3D printing. For single-point contacts, standard force sensors (HZC-MS1, Cy Sensors, China) with a force precision of 0.03 N were integrated into the grippers to collect ground truth force data. For multiple-point contacts, another nine standard force sensors (DYHW-108, Dayang Sensors, China) were integrated into two types of grippers to collect truth data, as shown in fig. S14. Considering that the PhyTac exhibits 3D axial symmetry, data collection is only required for markers between two adjacent columns. This platform can automatically traverse the selected columns by applying different force values under quasi-static conditions and can automatically and simultaneously record the ground truth force distribution and the corresponding dynamic image from the camera. Furthermore, we also established a validation platform to collect data of real hand grip (fig. S16). This platform includes nine standard force sensors (DYHW-108), which are distributed across five fingers of a glove. Wearing this glove, we gripped the PhyTac in different grip orientations, positions, and directions to collect data and verify its robustness and generalizability.

Calibration of the FEM model and the cascade neural network

The parameters of FEM (Young's modulus, Poisson's ratio, etc.) of the outer shell were calibrated on the basis of the collected force data. This calibration could be simplified as a minimization problem, expressed as follows

$$\min_p \left[\sum_{i=1, \dots, n} \|F_{gti} - K(p) \cdot U_i\| \right] \quad (4)$$

In this equation, p represents the parameters, F_{gt} the ground truth force, and n the number of samples. By minimizing the difference between the experimentally ground truth and FEM estimation, the calibrated FEM model could be used to estimate the force distribution (fig. S27). As for the cascade neural network, the collected data include 598 samples with random external force values, among which around 48% data are collected by multiple-point contacts and the other is collected by single-point contacts. The dataset is split into training, validation, and test sets with a ratio of 8.5:0.5:1. The neural network is composed of three layers (except for the input layer), with 10 hidden units in each of the two hidden layers, and the activation function of each hidden neuron is a linear unit.

Virtual scenarios setup for application of VR interactions

The 3D VR environment and objects were designed with Unity3D (Unity Technologies) on a laptop computer and were projected into the VR headset (Oculus Quest 2, Meta) through Oculus Link. In Unity3D, the interaction between the PhyTac and VR environment was facilitated through the Transmission Control Protocol (TCP). The bending of virtual finger and applied force were controlled by the distributed force of individual fingers on the PhyTac, while the location and orientation of the virtual hand were tracked by the hand-tracking function of the Oculus. Unity3D used sphere and capsule collision on a hand model to detect the object contact via Unity3D script execution. When the virtual hand was not in contact with virtual objects, the bending of virtual fingers was independently controlled by the real applied force of each finger. When the virtual hand contacted an object, the distribution of applied force in real world was directly projected onto the virtual object, thereby mimicking precise manipulations in reality. As for the virtual objects, the egg and the vase could be crushed when the total force reached 50 and 80 N respectively, and the deformation of the soft ball is achieved through mesh deformation when the distributed force is applied.

Robot teleoperation setup for application of human-robot interactions

The robotic hand (Hiwonder Technology Co. Ltd., China) was integrated with the robotic arm (E03-Pro, Han's Robot Co. Ltd., China) using a 3D-printed connector. The bending of the robotic hand's fingers was controlled by the force distribution on the PhyTac via the serial port communication. Concurrently, the position and orientation of the robotic arm's end were open-loop controlled by the IMU (IM948, Chenyi Electronic Co. Ltd., China), which is integrated into the top of the PhyTac. The computer first collects the IMU results via Bluetooth and then gives commands to the robotic arm via TCP after information processing.

Supplementary Materials

The PDF file includes:

Supplementary Text
Figs. S1 to S27
Tables S1 to S3
Legends for movies S1 to S5
References

Other Supplementary Material for this manuscript includes the following:

Movies S1 to S5

REFERENCES AND NOTES

- Q. Li, O. Kroemer, Z. Su, F. F. Veiga, M. Kabolli, H. J. Ritter, A review of tactile information: Perception and action through touch. *IEEE Trans. Robot.* **36**, 1619–1634 (2020).
- I. You, D. G. Mackanic, N. Matsuhisa, J. Kang, J. Kwon, L. Beker, J. Mun, W. Suh, T. Y. Kim, J. B.-H. Tok, Z. Bao, U. Jeong, Artificial multimodal receptors based on ion relaxation dynamics. *Science* **370**, 961–965 (2020).
- L. Chen, S. Karilanova, S. Chaki, C. Wen, L. Wang, B. Winblad, S.-L. Zhang, A. Özçelikçalle, Z.-B. Zhang, Spike timing-based coding in neuromimetic tactile system enables dynamic object classification. *Science* **384**, 660–665 (2024).
- Z. Liu, X. Hu, R. Bo, Y. Yang, X. Cheng, W. Pang, Q. Liu, Y. Wang, S. Wang, S. Xu, Z. Shen, Y. Zhang, A three-dimensionally architected electronic skin mimicking human mechanosensation. *Science* **384**, 987–994 (2024).
- C. Xu, Y. Wang, J. Zhang, J. Wan, Z. Xiang, Z. Nie, J. Xu, X. Lin, P. Zhao, Y. Wang, J. Zhang, C. Liu, N. Xue, W. Zhao, M. Han, Three-dimensional micro strain gauges as flexible, modular tactile sensors for versatile integration with micro- and macroelectronics. *Sci. Adv.* **10**, eadp6094 (2024).
- R. L. Klatzky, S. Lederman, "Intelligent exploration by the human hand" in *Dextrous Robot Hands*, S. T. Venkataraman, T. Iberall, Eds. (Springer, 1990; https://doi.org/10.1007/978-1-4613-8974-3_4), pp. 66–81.
- R. J. K. Jacob, Human-computer interaction: Input devices. *ACM Comput. Surv.* **28**, 177–179 (1996).
- R.-D. Vatavu, "Gesture-based interaction," in *Handbook of Human Computer Interaction*, J. Vanderdonckt, P. Palanque, M. Winckler, Eds. (Springer International Publishing, 2020; https://doi.org/10.1007/978-3-319-27648-9_20-1), pp. 1–47.
- R. W. McGorry, P. G. Dempsey, J. S. Casey, The effect of force distribution and magnitude at the hand-tool interface on the accuracy of grip force estimates. *J. Occup. Rehabil.* **14**, 255–266 (2004).
- L. Burnie, N. Chockalingam, A. Holder, T. Claypole, L. Kilduff, N. Bezodis, Commercially available pressure sensors for sport and health applications: A comparative review. *Foot* **56**, 102046 (2023).
- Y. Luo, Y. Li, P. Sharma, W. Shou, K. Wu, M. Foshey, B. Li, T. Palacios, A. Torralba, W. Matusik, Learning human–environment interactions using conformal tactile textiles. *Nat. Electron.* **4**, 193–201 (2021).
- Y. Shi, F. Wang, J. Tian, S. Li, E. Fu, J. Nie, R. Lei, Y. Ding, X. Chen, Z. L. Wang, Self-powered electro-tactile system for virtual tactile experiences. *Sci. Adv.* **7**, eabe2943 (2021).
- J. A. Barreiros, A. Xu, S. Pugach, N. Iyengar, G. Troxell, A. Cornwell, S. Hong, B. Selman, R. F. Shepherd, Haptic perception using optoelectronic robotic flesh for embodied artificially intelligent agents. *Sci. Robot.* **7**, eabi6745 (2022).
- Y. Yan, Z. Hu, Z. Yang, W. Yuan, C. Song, J. Pan, Y. Shen, Soft magnetic skin for super-resolution tactile sensing with force self-decoupling. *Sci. Robot.* **6**, eabc8801 (2021).
- J. Shi, Y. Dai, Y. Cheng, S. Xie, G. Li, Y. Liu, J. Wang, R. Zhang, N. Bai, M. Cai, Y. Zhang, Y. Zhan, Z. Zhang, C. Yu, C. F. Guo, Embedment of sensing elements for robust, highly sensitive, and cross-talk-free iontronic skins for robotics applications. *Sci. Adv.* **9**, eadf8831 (2023).
- H. C. Roberts, H. J. Denison, H. J. Martin, H. P. Patel, H. Syddall, C. Cooper, A. A. Sayer, A review of the measurement of grip strength in clinical and epidemiological studies: Towards a standardised approach. *Age Ageing* **40**, 423–429 (2011).
- S. Sundaram, P. Kellnhofer, Y. Li, J.-Y. Zhu, A. Torralba, W. Matusik, Learning the signatures of the human grasp using a scalable tactile glove. *Nature* **569**, 698–702 (2019).
- X.-M. Wang, L.-Q. Tao, M. Yuan, Z.-P. Wang, J. Yu, D. Xie, F. Luo, X. Chen, C. Wong, Sea urchin-like microstructure pressure sensors with an ultra-broad range and high sensitivity. *Nat. Commun.* **12**, 1776 (2021).
- Y. Tang, T. Zhang, H. Ren, W. Zhang, G. Li, D. Guo, L. Yang, R. Tan, Y. Shen, Highly sensitive spherical cap structure-based iontronic pressure sensors by a mold-free fabrication approach. *Smart Mater. Struct.* **31**, 095030 (2022).
- J. Li, H. Jia, J. Zhou, X. Huang, L. Xu, S. Jia, Z. Gao, K. Yao, D. Li, B. Zhang, Y. Liu, Y. Huang, Y. Hu, G. Zhao, Z. Xu, J. Li, C. K. Yiu, Y. Gao, M. Wu, Y. Jiao, Q. Zhang, X. Tai, R. H. Chan, Y. Zhang, X. Ma, X. Yu, Thin, soft, wearable system for continuous wireless monitoring of artery blood pressure. *Nat. Commun.* **14**, 5009 (2023).

21. J. Li, Y. Liu, M. Wu, K. Yao, Z. Gao, Y. Gao, X. Huang, T. H. Wong, J. Zhou, D. Li, H. Li, J. Li, Y. Huang, R. Shi, J. Yu, X. Yu, Thin, soft, 3D printing enabled crossstalk minimized triboelectric nanogenerator arrays for tactile sensing. *Fundam. Res.* **3**, 111–117 (2023).
22. W. Yuan, S. Dong, E. H. Adelson, GelSight: High-resolution robot tactile sensors for estimating geometry and force. *Sensors* **17**, 2762 (2017).
23. S. Wang, Y. She, B. Romero, E. Adelson, "GelSight wedge: Measuring high-resolution 3D contact geometry with a compact robot finger" in *2021 IEEE International Conference on Robotics and Automation (ICRA)* (IEEE, 2021; <https://ieeexplore.ieee.org/document/9560783>), pp. 6468–6475.
24. B. Ward-Cherrier, N. Pestell, L. Cramphorn, B. Winstone, M. E. Giannaccini, J. Rossiter, N. F. Lepora, The TacTip family: Soft optical tactile sensors with 3D-printed biomimetic morphologies. *Soft Robot.* **5**, 216–227 (2018).
25. L. Van Duong, V. A. Ho, Large-scale vision-based tactile sensing for robot links: Design, modeling, and evaluation. *IEEE Trans. Robot.* **37**, 390–403 (2021).
26. Q. K. Luu, N. H. Nguyen, V. A. Ho, Simulation, learning, and application of vision-based tactile sensing at large scale. *IEEE Trans. Robot.* **39**, 2003–2019 (2023).
27. H. Sun, K. J. Kuchenbecker, G. Martius, A soft thumb-sized vision-based sensor with accurate all-round force perception. *Nat. Mach. Intell.* **4**, 135–145 (2022).
28. W.-G. Kim, D.-W. Kim, I.-W. Tcho, J.-K. Kim, M.-S. Kim, Y.-K. Choi, Triboelectric nanogenerator: Structure, mechanism, and applications. *ACS Nano* **15**, 258–287 (2021).
29. Y. Chang, L. Wang, R. Li, Z. Zhang, Q. Wang, J. Yang, C. F. Guo, T. Pan, First decade of interfacial ionic sensing: From droplet sensors to artificial skins. *Adv. Mater.* **33**, 2003464 (2021).
30. H. Bai, S. Li, J. Barreiros, Y. Tu, C. R. Pollock, R. F. Shepherd, Stretchable distributed fiber-optic sensors. *Science* **370**, 848–852 (2020).
31. D. Ma, E. Donlon, S. Dong, A. Rodriguez, Dense Tactile Force Estimation using GelSlim and inverse FEM, in *2019 International Conference on Robotics and Automation (ICRA)* (2019), pp. 5418–5424.
32. C. Sferrazza, R. D'Andrea, Design, motivation and evaluation of a full-resolution optical tactile sensor. *Sensors* **19**, 928 (2019).
33. C. Sferrazza, R. D'Andrea, Sim-to-real for high-resolution optical tactile sensing: From images to three-dimensional contact force distributions. *Soft Robotics* **9**, 926–937 (2022).
34. A. Handler, D. D. Ginty, The mechanosensory neurons of touch and their mechanisms of activation. *Nat. Rev. Neurosci.* **22**, 521–537 (2021).
35. N. L. Neubarth, A. J. Emanuel, Y. Liu, M. W. Springel, A. Handler, Q. Zhang, B. P. Lehnert, C. Guo, L. L. Orefice, A. Abdelaziz, M. M. DeLisle, M. Iskols, J. Rhyns, S. J. Kim, S. J. Cattel, W. Regehr, C. D. Harvey, J. Drugowitsch, D. D. Ginty, Meissner corpuscles and their spatially intermingled afferents underlie gentle touch perception. *Science* **368**, eabb2751 (2020).
36. D. Reinhardt, E. M. Gola, Law and order in plants—The origin and functional relevance of phyllotaxis. *Trends Plant Sci.* **27**, 1017–1032 (2022).
37. S. Strauss, J. Lempe, P. Prusinkiewicz, M. Tsiantis, R. S. Smith, Phyllotaxis: Is the golden angle optimal for light capture? *New Phytol.* **225**, 499–510 (2020).
38. R. W. Pearcy, W. Yang, The functional morphology of light capture and carbon gain in the Redwood forest understorey plant *Adenocaulon bicolor* Hook. *Funct. Ecol.* **12**, 543–552 (1998).
39. S. King, F. Beck, U. Lüttge, On the mystery of the golden angle in phyllotaxis. *Plant Cell Environ.* **27**, 658–695 (2004).
40. N. J. Seo, T. J. Armstrong, Investigation of grip force, normal force, contact area, hand size, and handle size for cylindrical handles. *Hum. Factors* **50**, 734–744 (2008).
41. H. Wang, W. Wang, J. J. Kim, C. Wang, Y. Wang, B. Wang, S. Lee, T. Yokota, T. Someya, An optical-based multipoint 3-axis pressure sensor with a flexible thin-film form. *Sci. Adv.* **9**, eadi2445 (2023).
42. S. Herbort, A. Grumpe, C. Wöhler, Reconstruction of non-Lambertian surfaces by fusion of Shape from Shading and active range scanning, in *2011 18th IEEE International Conference on Image Processing* (2011), pp. 17–20.
43. E. Oñate, "Thick/thin plates. Reissner-Mindlin theory" in *Structural Analysis with the Finite Element Method Linear Statics: Volume 2. Beams, Plates and Shells*, E. Oñate, Ed. (Springer Netherlands, 2013; https://doi.org/10.1007/978-1-4020-8743-1_6) *Lecture Notes on Numerical Methods in Engineering and Sciences*, pp. 291–381.
44. G. E. Karniadakis, I. G. Kevrekidis, L. Lu, P. Perdikaris, S. Wang, L. Yang, Physics-informed machine learning. *Nat. Rev. Phys.* **3**, 422–440 (2021).
45. J. E. Mottershead, M. I. Friswell, Model updating in structural dynamics: A survey. *J. Sound Vib.* **167**, 347–375 (1993).
46. F. Salaffi, M. Carotti, S. Farah, L. Ceccarelli, M. Di Carlo, Handgrip strength features in rheumatoid arthritis patients assessed using an innovative cylindrical-shaped device: Relationships with demographic, anthropometric and clinical variables. *J. Med. Syst.* **45**, 100 (2021).
47. K. Zhang, K. Zhang, L. Wang, The evaluation of sports performance in tennis based on flexible piezoresistive pressure sensing technology. *IEEE Sens. J.* **24**, 28111–28118 (2024).
48. D. Chadeaux, G. Rao, J.-L. Le Carrou, E. Berton, L. Vigouroux, The effects of player grip on the dynamic behaviour of a tennis racket. *J. Sports Sci.* **35**, 1155–1164 (2017).
49. J. Romero, D. Zionas, M. J. Black, Embodied hands: Modeling and capturing hands and bodies together. *ACM Trans. Graph.* **36**, 245 (2017).
50. J. Desrosiers, R. Hébert, G. Bravo, E. Dutil, Comparison of the Jamar dynamometer and the Martin vigorimeter for grip strength measurements in a healthy elderly population. *J. Rehabil. Med.* **27**, 137–143 (1995).
51. J. A. Balogun, S. A. Adenlola, A. A. Akinloye, Grip strength normative data for the harpenden dynamometer. *J. Orthop. Sports Phys. Ther.* **14**, 155–160 (1991).
52. M. Lambeta, P.-W. Chou, S. Tian, B. Yang, B. Maloon, V. R. Most, D. Stroud, R. Santos, A. Byagowi, G. Kammerer, D. Jayaraman, R. Calandra, DIGIT: A novel design for a low-cost compact high-resolution tactile sensor with application to in-hand manipulation. *IEEE Robot. Autom. Lett.* **5**, 3838–3845 (2020).
53. B. Winstone, C. Melhuish, T. Pipe, M. Callaway, S. Dogramadzi, Toward bio-inspired tactile sensing capsule endoscopy for detection of submucosal tumors. *IEEE Sens. J.* **17**, 848–857 (2017).
54. D. F. Gomes, Z. Lin, S. Luo, "GelTip: A finger-shaped optical tactile sensor for robotic manipulation" in *2020 IEEE/RSJ International Conference on Intelligent Robots and Systems (IROS)* (IEEE, 2020), pp. 9903–9909.
55. A. Padmanabha, F. Ebert, S. Tian, R. Calandra, C. Finn, S. Levine, "OmniTact: A multi-directional high-resolution touch sensor" in *2020 IEEE International Conference on Robotics and Automation (ICRA)* (IEEE, 2020), pp. 618–624.
56. T. Q. Dinh, J. I. Yoon, J. Marco, P. Jennings, K. K. Ahn, C. Ha, Sensorless force feedback joystick control for teleoperation of construction equipment. *Int. J. Precis. Eng. Manuf.* **18**, 955–969 (2017).
57. S. Li, R. Rameshwar, A. M. Votta, C. D. Onal, Intuitive control of a robotic arm and hand system with pneumatic haptic feedback. *IEEE Robot. Autom. Lett.* **4**, 4424–4430 (2019).
58. D. Leonardis, M. Gabardi, S. Marcheschi, M. Barsotti, F. Porcini, D. Chiaradia, A. Frisoli, Hand teleoperation with combined kinaesthetic and tactile feedback: A full upper limb exoskeleton interface enhanced by tactile linear actuators. *Robotics* **13**, 119 (2024).
59. K. Fujimoto, F. Kobayashi, H. Nakamoto, F. Kojima, "Development of haptic device for five-fingered robot hand teleoperation" in *Proceedings of the 2013 IEEE/SICE International Symposium on System Integration* (IEEE, 2013; <https://ieeexplore.ieee.org/document/6776746>), pp. 820–825.
60. D. S. Pamungkas, K. Ward, "Tele-operation of a robot arm with electro tactile feedback" in *2013 IEEE/ASME International Conference on Advanced Intelligent Mechatronics* (IEEE, 2013; <https://ieeexplore.ieee.org/document/6584175>), pp. 704–709.

Acknowledgments: We acknowledge C. Thorogood from the University of Oxford Botanic Garden and Arboretum for providing the photo of *Aloe polyphylla* in Fig. 1B. **Funding:** This work was supported by Hong Kong RGC General Research Fund (16203923) and Guangdong Basic and Applied Basic Research Foundation (GDST24EG02). **Author contributions:** Conceptualization: Y.S. and Y.T.; methodology: Y.T., G.L., and Y.S.; software: Y.T. and G.L.; validation: Y.T., G.L., T.Z., H.R., X.Y., L.Y., D.G., and Y.S.; formal analysis: Y.T. and Y.S.; data curation: Y.T. and G.L.; visualization: Y.T., T.Z., H.R., X.Y., L.Y., and G.D.; writing—original draft preparation: Y.T. and Y.S.; writing—review and editing: Y.T. and Y.S.; supervision: Y.S.; project administration: Y.S.; funding acquisition: Y.S. All authors have read and agreed to the published version of the manuscript. **Competing interests:** The authors declare that they have no competing interests. **Data and materials availability:** All data needed to evaluate the conclusions in the paper are present in the paper and/or the Supplementary Materials.

Submitted 19 September 2024

Accepted 18 December 2024

Published 22 January 2025

10.1126/sciadv.adt2641